Article

Journal of Vibration and Control
2024, Vol. 30(19-20) 4438–4449

DOI: 10.1177/10775463231210031
journals.sagepub.com/home/jvc
Sage

Active noise control with resonant flush-mounted piezoelectric cells in the presence of airflow: Wind tunnel experiments

Jonathan Rodriguez[1], Mouhamed Ezzine[2], Manuel Collet[2], and Vincent Clair[2]

Abstract

Methods and technologies to control the noise coming from turbulent flows impinging on outlet guide vanes in turbofan engines are tremendously needed nowadays to comply with new legislation on acoustic environment pollution. The following paper relies on preliminary research proposing a new experimental design of active noise control system to be further integrated into a jet engine outer guide vane prototype, consisting of multiple flush-mounted piezoelectric cells. Here, three active cells are placed on the bottom wall of a wind tunnel with upstream acoustic excitation generating grazing incident waves for different airflow velocities. Using a downstream microphone as an error sensor, the active system succeeds in improving the transmission loss of the sample by 2.5 dB at the target frequency (670 Hz) corresponding to the main piezo acoustic mode with airflow velocities up to 20 m.s^{-1}. These early experimental results confirm the ability of the concept to interact with the ambient acoustics without disturbing the airflow as in passive solutions using porous materials, for instance, leading the path to future experiments with realistic turbulence generating acoustic sources on the leading edge of the vane profile.

Keywords

Active noise control, outlet guide vane, grazing incidence, turbofan engine

1. Introduction

In the past years, international regulations have become more and more severe regarding environmental noise pollution. With the increase of air traffic around airports, aircraft noise pollution has logically become a major concern, and methods and technologies to address this problem are concentrating a lot of effort from manufacturers and researchers. Thus, the main objective of these new noise control systems is to reduce the noise emitted by turbofan engines as mentioned by Desquesnes et al. (2007) due to airflow-airfoil interactions inside the jet engine nacelle.

One of the main noise sources comes from the fluid/structure interaction between vortices created by the rotor blades passing and the leading edge of the stator vanes or outlet guide vanes (OGV) located downstream. To achieve significant noise attenuation at the stator level, three methods are available (Envia, 2002; Neise and Enghardt, 2003; Huff, 2007; Liu et al., 2022): geometry optimization, passive control materials, and active control.

Applied to vanes profiles, geometry optimization solutions include swept and/or leaned stator as mentioned by Envia et al. (1996) and serrations on the leading or trailing edge as in the work from Hansen et al. (2012) and Vemuri et al. (2020). In passive structural acoustic control, softer vanes or acoustic liners at the inlet of turbofan engines (Eldredge and Dowling, 2003) can be used to add noise dissipation to the structure. Just like in the work from Geyer et al. (2010), a very common solution is the use of porous materials with cavities of different size acting as Helmholtz resonators that can provide excellent noise attenuation for both tonal and broadband disturbance. Although widely used, these materials often represent a non-negligible

[1]Univ Lyon, CNRS, INSA Lyon, Villeurbanne, France
[2]Université de Lyon, Ecole Centrale de Lyon, Ecully, France

Received: 31 May 2023; revised: 15 September 2023; accepted: 9 October 2023

Corresponding author:
Jonathan Rodriguez, Univ Lyon, CNRS, INSA Lyon, LaMCoS, UMR5259, Villeurbanne 69621, France.
Email: jonathan.rodriguez@insa-lyon.fr

additional weight and volume inside the structure. Moreover, such modifications of airfoil geometry or boundary layer can also result in noise amplification at particular conditions and degradation of aerodynamic performance which is the most severe consequence.

Thus, active stator vanes can be considered relevant technological solutions for their lightweight and closeness to the noise source, providing the theoretical opportunity to reduce by 80% the downstream radiated noise as demonstrated by Vinogradov and Zhou (2014). However, two major difficulties arise from the location of the actuators: many of the acoustic control problems, especially when optimizing the transmission loss are addressed with normal wave incidence (Carneal et al., 2008 and Ripamonti et al., 2022), giving maximum control authority to actuators oriented directly toward the acoustic wave velocity vector.

In addition, for experiments within ducts including or not airflow (Carmona and Alvarado, 2000), the control actuators are in general loudspeakers, which facilitate the control of the acoustic field for obvious physical reasons. Nevertheless, these actuators are heavy and require a certain available volume to be implemented. This last constraint is not consistent with the considered thin OGV profiles inside the turbofan engine.

Early attempts have been made to implement piezoelectric transducers at the surface of OGVs with the objective of acoustic control. For instance, Curtis (1999) used flush-mounted PZT-5A transducers on stator vanes. A 3–6 dB attenuation for tonal excitation was achieved with transducers supplied by 150 V. Besides, the authors pointed out the difficulty to obtain sufficient acoustic controllability with this type of thin actuator.

Galland et al. (2005) and Sellen et al. (2006) developed hybrid actuators with a piezoelectric transducer driving a membrane inside a small cavity. Combining the high-frequency performance of the passive part and the low-frequency performance of the active one, up to 20 dB gain on the transmission loss (TL) was achieved within a duct with different airflow velocities. Still, the volume necessary for the actuator, its membrane flexibility, and its wire mesh surface structure are not compatible with our specific need for a flush-mounted control system for a thin OGV profile to not disturb the flow and maintain static pressure.

Hence, the following research work proposes preliminary experimental results on a new proposition of an active noise control system dedicated to reducing the acoustic emission from the interaction turbulence/airfoil on the leading edge of stator vanes. To this end, the system prototype is placed at the bottom wall of a wind tunnel with an additional upstream acoustic source. The concept consists of flush-mounted piezoelectric cells optimized in their design to take advantage of their main electromechanical resonance and control the noise within the desired bandwidth on a downstream target microphone within the duct.

The paper is organized as follows: Section 2 presents the prototype design with its electromechanical and electro-acoustical behavior. Then Section 3 details the experimental setup with the acoustic and airflow duct. The Section 4 develops the identification process and the active control design. Finally, Section 5 addresses the experimental results obtained in terms of transmission and insertion loss thanks to the active control system.

2. Active flush-mounted cells design

The present section introduces the prototype mechanical design initiated by Perez et al. (2020) and the electro-acoustical behavior of the cells within the experimental setup of the wind tunnel. As mentioned earlier, the proposed active noise control system is aimed to reduce the noise level emitted by the interaction between a turbulent airflow coming from the rotor vanes and the airfoil surface of the OGV.

The functioning principle of the cells is depicted in the Figures 1 and 2. Thus, each piezoelectric cell is constituted by a thin 1 mm aluminum skin of 44 × 44 mm with six transducers fixed with epoxy resin and connected in parallel. The transducers, in green color, are PZT-5A piezoelectric stack of 10 × 5 mm section and 2 mm thickness in the strain direction (d_{33}). The mechanical mounting wedges have been optimized to improve the effective piezo acoustic coupling. The main idea is to design a high-frequency acoustic actuator by maximizing the moving surface of the cell for a certain bandwidth and also the electromechanical coupling. Since the aluminum skin remains rigid, additional steel masses of 168 g have been added to guarantee sufficient electromechanical coupling within the desired bandwidth.

The manufactured prototype of the outer vane profile consists of three operational flush-mounted piezoelectric cells to be installed in a wind tunnel for preliminary experiments as displayed in Figure 3. Unfortunately, cells #4 and #5 presented electromechanical issues during the experiment due to the manufacturing process, and were disconnected to not disturb the dynamic behavior of the remaining operational cells #1–#3.

3. Experimental setup

The operational prototype cells are installed in a wind tunnel with a rectangular section of 68 × 110 mm. Figure 4 provides a schematic representation of the experimental setup in addition with pictures in Figure 5. First, a constant airflow, controllable in velocity enters the tunnel through an inlet section and goes out through an anechoic outlet. At the upstream section and isolated from the airflow, a loudspeaker is used as an external acoustic source. The active cells are then positioned at the reference position $x = 0$ and four microphones measure the acoustic pressure at positions

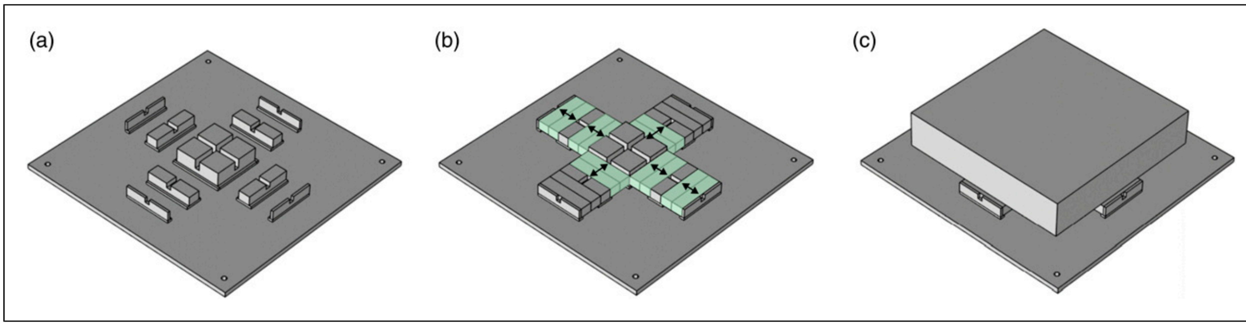

Figure 1. 3D representations of each piezoelectric cell architecture: (a) aluminum skin alone, (b) six operational transducers (green color) with their main strain direction under electric excitation, and (c) additional mass.

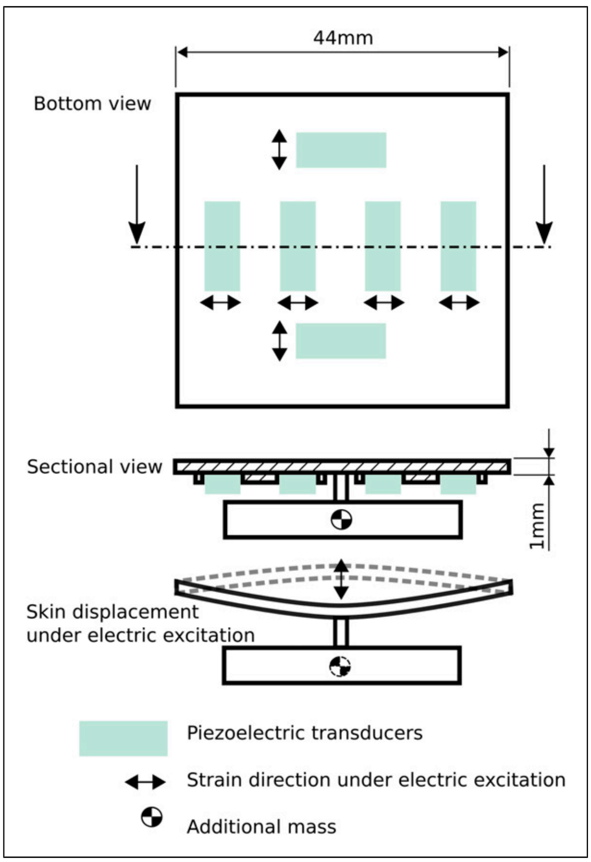

Figure 2. Schematic representation of the piezoelectric transducers implementation on each cell and operational deformation under electric excitation.

upstream (x_1 and x_2) and downstream (x_3 and x_4). The microphone positions are given in Table 1. Since the reference duct has almost no acoustic reflection, these four microphones are dedicated to estimating the transmission loss (TL) of the active prototype.

Considering the active control part, the error microphone is selected to be the #3. Thus, it is connected to both the acquisition system and a dSPACE MicroLabBox controller. The controller then generates a voltage command signal

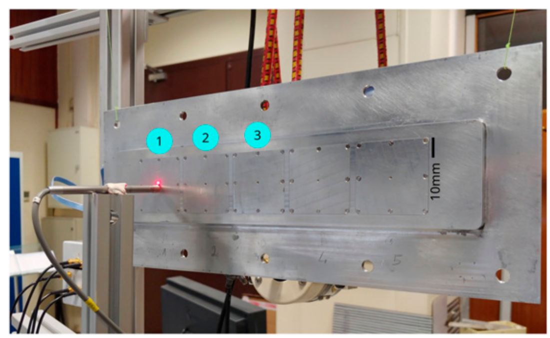

Figure 3. Active noise control system overview with operational cells #1–#3 and scale (system not installed yet inside the wind tunnel).

of +/− 10 V for each active cell which is amplified by a 10× gain through a voltage amplifier, leveling up the piezoelectric supply voltage to +/− 100 V. Finally, the following acoustic control experiment is realized using an airflow velocity inside the duct between 0 and 20 m.s^{-1} (Mach 0.06).

4. System identification and control

The following section describes the identification process of the piezo acoustic system between the cell voltage command signals and the error microphone response without airflow. Then, a modal-shaped LQG controller is derived to target the maximum acoustic controllability bandwidth of the control system.

4.1. Piezo acoustic system response

First, the multi single-input/single-output (MSISO) control system considered is defined and a schematic representation is displayed on Figure 6. Hence, $y(t)$ is the microphone output signal (error signal). The transfer functions $H_{ij}(s)$ with $s = \mathbf{j}\omega$ as the Laplace variable, define the effect of actuator i on sensor j with $i \in \{1, 2, 3\}$ and $j \in \{1, 2\}$ (1 for microphone and 2 for the laser vibrometer). The controller

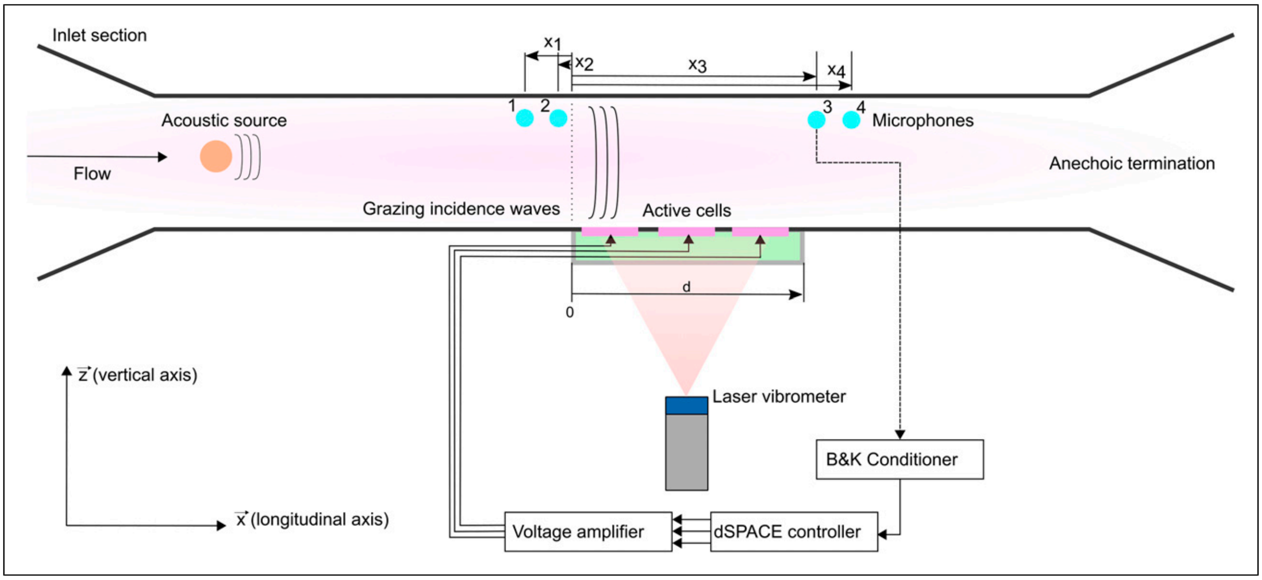

Figure 4. Wind tunnel experiment schematic representation.

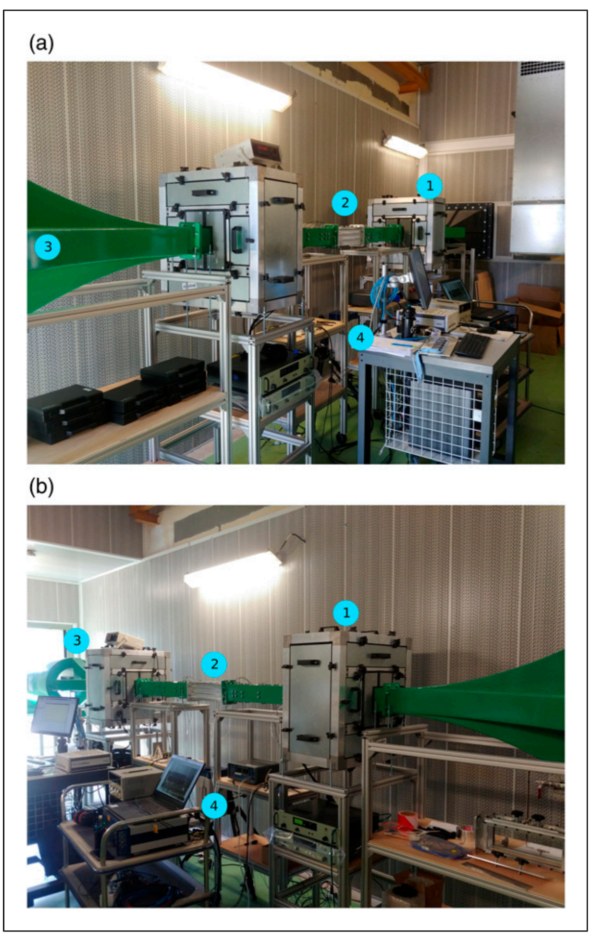

Figure 5. Wind tunnel experiment: (a) view from downstream and (b) view from upstream, (1) acoustic source, (2) active sample, (3) anechoic outlet, and (4) laser vibrometer.

Table 1. Microphones positions inside the duct and active sample length.

Microphone	Position (mm)
x_1	-135
x_2	-100
D	453
x_3	550
x_4	585

transfer functions are then defined by $K_i(s)$ and their output control signal $u_i(t)$.

The frequency response functions (FRF) measurement of the error microphone responses to the excitation of the control system is realized by sending to each one of the active cells a band-limited white noise with a sampling frequency of 50 kHz and maximum amplitude 10 V. In addition, a Polytec PSV500 laser vibrometer measures from behind the cells the mechanical vibration of the active aluminum surfaces to observe the electromechanical coupling of the system and compare it to the piezo acoustic coupling characterizing its performance.

The measured FRFs $H_{i1}(f)$, $H_{i2}(f)$, and their spectral coherence are displayed on the Figures 7–9, respectively. One can clearly notice that each cell has a different acoustic impact on the environment in the frequency domain. Cell #1 presents a main electro-acoustic mode at $f_1 = 450\ Hz$, cell #2 has the lowest coupling and acts at 470 Hz and 610 Hz. Finally, cell #3 shows the best piezo acoustic coupling at 670 Hz. Besides, the measured FRFs $H_{i2}(f)$, when compared to their acoustic counterpart $H_{i1}(f)$ present higher amplitudes and better spectral coherence for a larger bandwidth. This major observation demonstrates that although the system is well designed with a good electromechanical coupling with this configuration of piezoelectric transducers, it still must be optimized further to generate more acoustic pressure on the aluminum skin surface to improve the piezo acoustic coupling. The observed discrepancies between all piezoelectric cells come from small differences occurring during wedges manufacturing and piezoelectric layer gluing. One can also underline the main importance of the membrane clamping that modifies the frequency of the main electromechanical mode. This sensitivity shall be considered in future optimization and design.

Nonetheless, a modal model of the functions $H_{i1}(s)$ is defined using the same methodology and formalism as Rodriguez et al. (2021) assuming the target modes are sufficiently separated in frequency. Hence, the approximation $\widehat{H}_{i1}(s)$ is of the form:

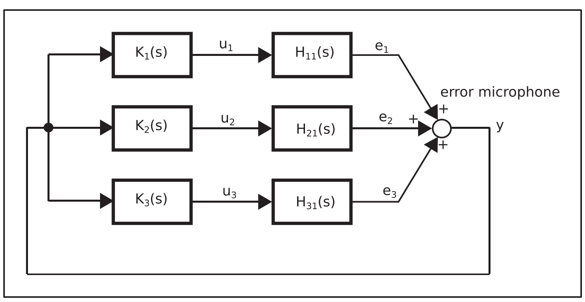

Figure 6. Control problem scheme.

$$\widehat{H}_{i1}(s) = \sum_{k=1}^{n} \frac{a_k^{i1} + b_k^{i1} s}{s^2 + \omega_k^2 + 2\xi_k \omega_k s} \tag{1}$$

where $k \in [1; n]$ is the target mode number, $\omega_k \in \mathbb{R}^{+*}$ is the mode frequency in rad.s^{-1}, $\xi_k \in \mathbb{R}^+$ is the mode damping and $(a_k^{i1}, b_k^{i1}) \in \mathbb{R}^2$ are correction coefficients to obtain the right modal amplitude and phase at ω_k such that:

$$a_k^{i1} = Re\{H_{i1}(\mathbf{j}\omega_k) \times 2\xi_k \mathbf{j}\omega_k^2\} \tag{2}$$

$$b_k^{i1} = \frac{1}{\omega_k} \times Im\{H_{i1}(\mathbf{j}\omega_k) \times 2\xi_k \mathbf{j}\omega_k^2\} \tag{3}$$

The results of this identification process are summarized in Table 2 and the corresponding estimated functions $\widehat{H}_{i1}(f)$ are displayed in Figure 10. This modal model approximation is especially valid in this context since the controllability of each cell on the error sensor is very narrow in the frequency domain.

4.2. Control design

For control purpose, a state-space realization is then defined for $\widehat{H}_{i1}$ as:

$$\widehat{H}_{i1} \begin{cases} \dot{x}_i = A_i x_i + B_i u_i \\ e_i = C_i x_i \end{cases} \tag{4}$$

with $A_i \in \mathbb{R}^{2n \times 2n}$, $B_i \in \mathbb{R}^{2n \times 1}$, $C_i \in \mathbb{R}^{1 \times 2n}$, and $x_i \in \mathbb{R}^{2n}$ ($D_i = 0$ since $\widehat{H}_{i1}$ is strictly proper). The matrices of the aforementioned state-space system are defined by:

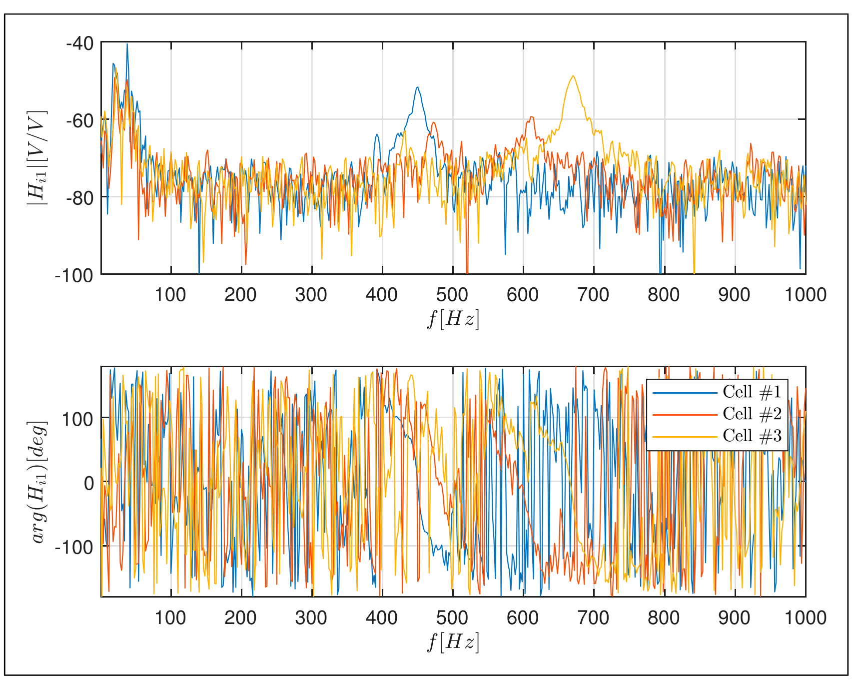

Figure 7. Measured FRF $H_{i1}(f)$ from each cell to error microphone.

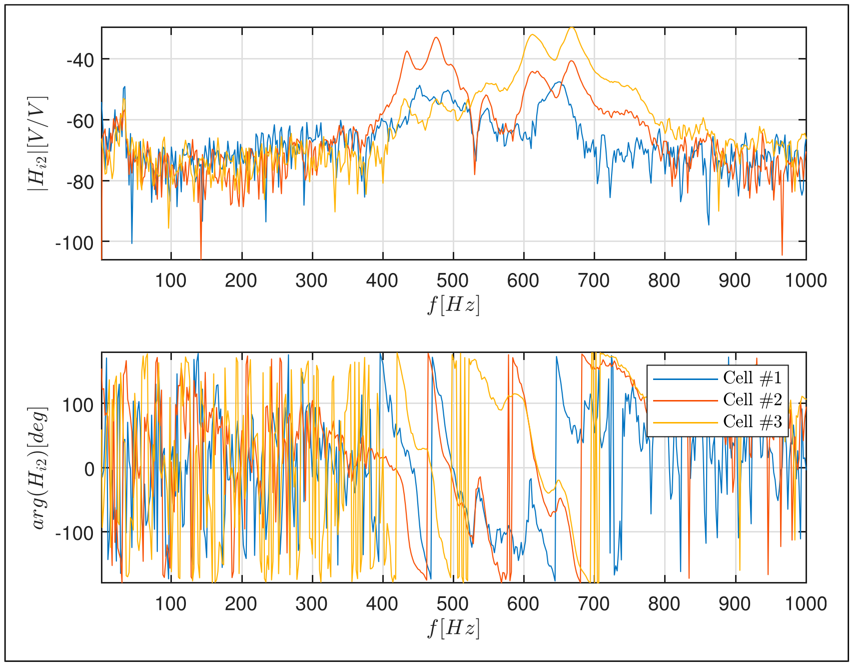

Figure 8. Measured FRF $H_{i2}(f)$ from each cell to laser vibrometer.

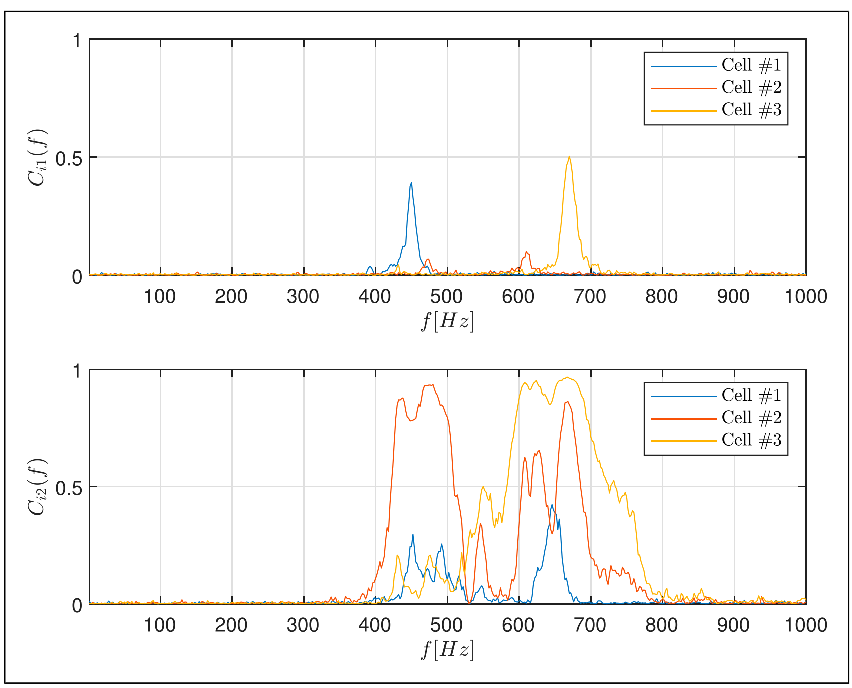

Figure 9. Measured spectral coherences $C_{i1}(f)$ and $C_{i2}(f)$.

$$A_i = \begin{bmatrix} 0_n & I_n \\ -diag(\omega_k^2) & -2diag(\xi_k\omega_k) \end{bmatrix}_{2n,2n} \quad (5)$$

$$B_i = [0_{1,n} \ 1_{1,n}]^T \quad (6)$$

$$C_i = [a_1^{i1} \cdots a_n^{i1} \ b_1^{i1} \cdots b_n^{i1}] \quad (7)$$

Now that the system is modeled with a state-space representation, the state vector is augmented with a narrow band-pass filter F_i allowing the control from cell #i to focus on the target modes with a tunable bandwidth. Hence, the filter F_i is defined as:

$$F(s) = \frac{1}{1 + s^2/\omega_{LP}^2 + s/(Q_f\omega_{LP})} \times \frac{s^2/\omega_{HP}^2}{1 + s^2/\omega_{HP}^2 + s/(Q_f\omega_{HP})} \quad (8)$$

Table 2. Identification parameters.

Cell #	$\omega/(2\pi)$ (Hz)	ξ	a^{i1}	b^{i1}
1	450	0.01	71.45	0.16
2	472	0.015	−186.23	0.04
	612	0.015	440.18	0.01
3	670	0.01	724.14	0.26

where Q_f is the quality factor and the frequency parameters $(\omega_{HP}, \omega_{LP})$ define the control bandwidth. The system F_i directly filters the measure y and has the following state-space representation:

$$F_i \begin{cases} \dot{x}_F = A_F x_F + B_F y \\ y_F = C_F x_F \end{cases} \quad (9)$$

with $A_F \in \mathbb{R}^{m\times m}$, $B_F \in \mathbb{R}^{m\times 1}$, $C_F = I_m$ for the sake of simplicity and $x_F \in \mathbb{R}^m$, m depending on the order of F_i. Hence, the augmented system G_{i1} formed by F_i and $\widehat{H}_{i1}$ is written as:

$$\begin{bmatrix} \dot{x}_i \\ \dot{x}_F \end{bmatrix} = \begin{bmatrix} A_i & 0 \\ B_F C_i & A_F \end{bmatrix} \begin{bmatrix} x_i \\ x_F \end{bmatrix} + \begin{bmatrix} B_i \\ 0 \end{bmatrix} u_i \quad (10)$$

$$y_F = [0 \ C_F] \begin{bmatrix} x_i \\ x_F \end{bmatrix} \quad (11)$$

Equivalent to:

$$G_{i1} \begin{cases} \dot{x}_G = A_G x_G + B_G u_i \\ y_F = C_G x_G \end{cases} \quad (12)$$

with

$$x_G = \begin{bmatrix} x_i \\ x_F \end{bmatrix}, A_G = \begin{bmatrix} A_i & 0_{2n\times m} \\ B_F C_i & A_F \end{bmatrix}, \quad B_G = \begin{bmatrix} B_i \\ 0_{m\times 1} \end{bmatrix}, C_G = [0_{m\times 2n} \ C_F] \quad (13)$$

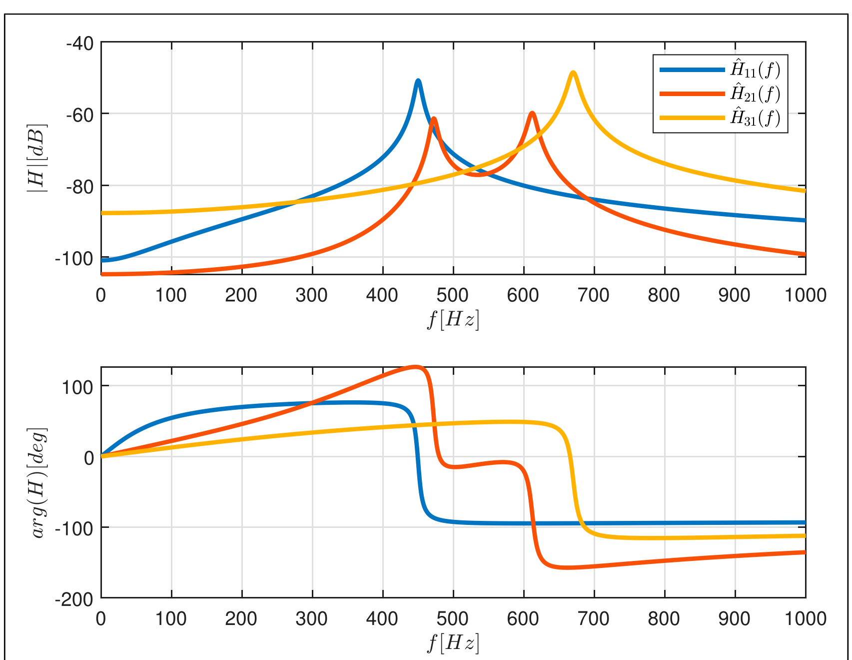

Figure 10. Modal models $\widehat{H}_{i1}(f)$ of measured transfer functions $H_{i1}(f)$ $\forall i \in [1:3]$.

The control gain matrix $M_i \in \mathbb{R}^{1\times(2n+m)}$ such that $u_i = -M_i x_G$ is finally computed for each cell as solution to the LQR problem (A_G, B_G) minimizing the following functional:

$$J = \frac{1}{2}\int_{-\infty}^{+\infty} x_G^T Q x_G + u_i^T R u_i \tag{14}$$

with $Q = diag([0_{1,2n}\ 1_m]) \times 10^2$ to control essentially within the bandwidth driven by F_i and $R = 10^{-4}$. Since only partial feedback is available from the filter output y_F, a Kalman filter is designed to estimate the full state x_G and the total controller is written as:

$$\dot{\hat{x}}_G = A_G\hat{x}_G + B_G u_i + L(y_G - C_G\hat{x}_G) \tag{15}$$

$$u_i = -M_i\hat{x}_G \tag{16}$$

where $\hat{x}_G$ is the state estimation. The observer gain matrix $L \in \mathbb{R}^{(2n+m)\times m}$ is computed considering a high level covariance in the state perturbation, allowing faster convergence to the real state. A scheme of the final controller K_i architecture is displayed on Figure 11.

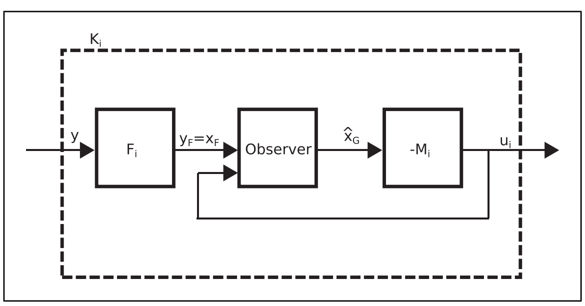

Figure 11. Controller K_i architecture.

5. Experimental results

This final section presents the results obtained in terms of active acoustic control in the experimental setup considered for airflow velocities up to 20 m.s^{-1} in the wind tunnel. As primary acoustic perturbation, a band-limited white noise is applied to a loudspeaker amplifier at a sampling frequency of 50 kHz (see Figure 4) with the actuator positioned upstream with respect to the active device. For each airflow velocity, the active noise control system is then switched on to observe its performance.

The Figures 12 and 13 display first the power spectral density (PSD) of the voltage signals coming from the downstream microphone #3 and upstream microphone #2, respectively, for all the experimental cases of control and airflow. One can immediately notice the low-frequency impact (see zoom section under 100 Hz) of the airflow within the duct. This observation is very positive since the control must operate at higher frequencies. Hence, the airflow should not interfere with the three control closed loops. The zoom section around the narrow bandwidth impacted by the control (620–712 Hz) confirms the previous conclusion since the control effect on the PSD of both downstream and upstream microphones is indeed not affected by the flow velocity. In terms of performance, a maximum attenuation of 4 dB is achieved on microphone #3, and only around 670 Hz demonstrating that the cells #1 and #2 are almost inefficient compared to cell #3. As mentioned earlier, there is still a lot of dispersion in the manufacturing process of the proposed prototypes, creating discrepancies in the electromechanical behavior. Besides, the acoustic level within the controlled bandwidth is increased upstream by the same attenuation factor at the downstream positions. Nevertheless, this level of attenuation is still interesting as it mainly demonstrates the physical and technological ability of the system to interact

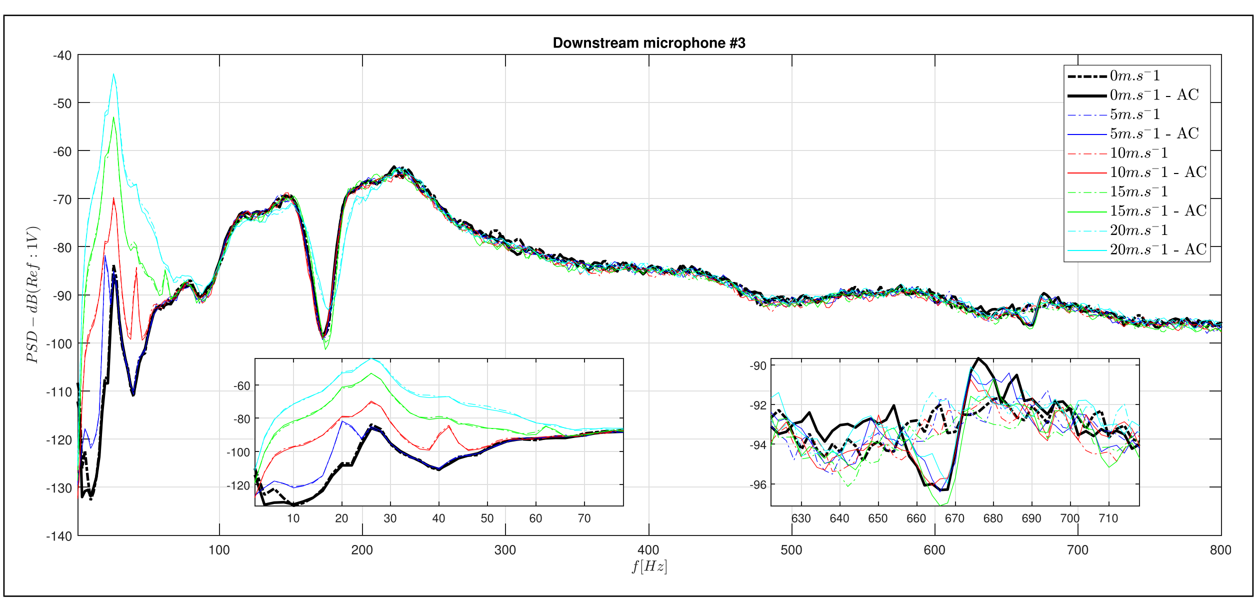

Figure 12. Downstream microphone #3 signal PSD for all values of airflow velocity, AC: Active Control.

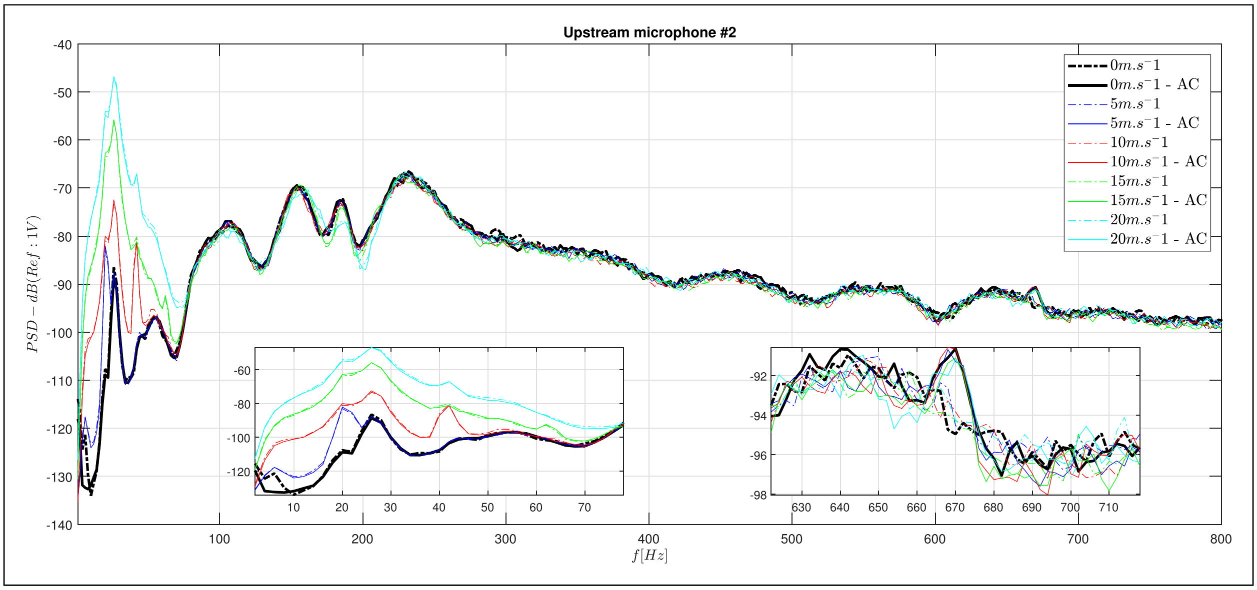

Figure 13. Upstream microphone #2 signal PSD for all values of airflow velocity, AC: Active Control.

with grazing incidence acoustic waves and impact the global downstream acoustic field.

Now the transmission loss (TL) representing the ratio between the incident sound power on the sample and the sound power transmitted by the sample can be computed:

$$TL = 10log_{10}\left(\left|\frac{A}{C}\right|^2\right) \tag{17}$$

where A and C are the complex coefficients of the transmission matrix (Ingard and Dear, 1985) corresponding to the incident waves. Then, the insertion loss (IL) representing the difference between the TL of the reference rigid liner and the TL from the considered control system is:

$$IL = TL - TL_{ref} \tag{18}$$

Figure 14 displays the estimation of the insertion loss (IL). Hence, a 2.5 dB gain is achieved by the proposed piezoelectric active control system around the main controlled frequency of 670 Hz on the IL, providing good confidence in this technological solution to control future acoustic sources coming from the interaction between turbulence and airfoil. Finally, the RMS values of the voltage control signal of each cell, for every airflow velocity are displayed in Figure 15. As observed previously, the actual airflow had no impact on the control bandwidth and the necessary control energy is not affected. A time domain extract of the control signal $u_1(t)$ with the extreme cases of airflow velocity is also plotted to illustrate this phenomenon.

5.1. Comparison with a passive solution

A passive solution to reduce noise emission due to the interaction between the turbulent flow and airfoil is being developed within the same project. Its design relies on the previous work from Bampanis et al. (2022). The passive cell used as a reference here is constituted of a 3.5 *mm* thick melamine foam for the porous material in addition to a metallic wire mesh with 0.02 *mm* apertures in contact with the airflow.

Five samples are placed in the wind tunnel as in Figure 4, using the same sample holder dimensions as the one presented in Figure 3, and the IL is measured. For comparison, Figure 16 displays the measured IL without airflow for both passive and active systems. One can clearly notice that the passive solution achieves a moderate broadband performance on the IL while the presented active prototype displays a higher level of IL, but over a very narrow

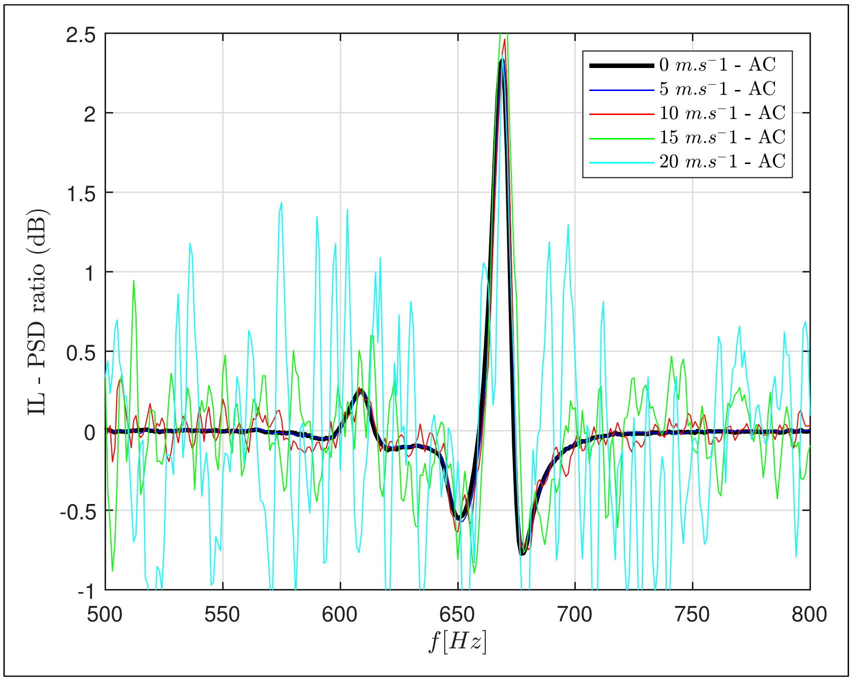

Figure 14. Insertion loss approximation in [dB] between the downstream microphones (#3 and #4) and the upstream microphones (#1 and #2) for all values of airflow velocity.

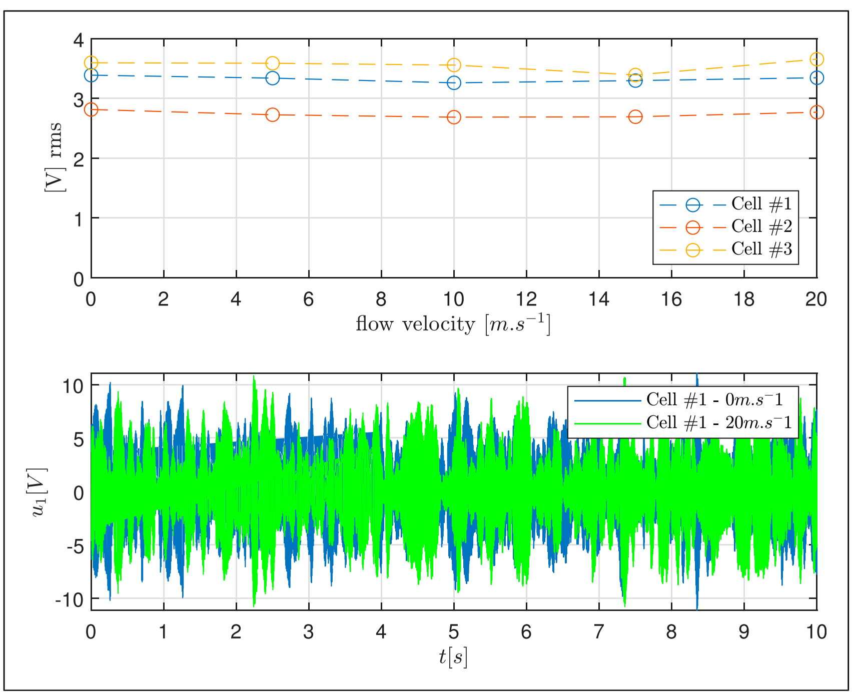

Figure 15. Control signal RMS value for each cell and all values of airflow velocity, $u_1(t)$ with no airflow and maximum velocity airflow.

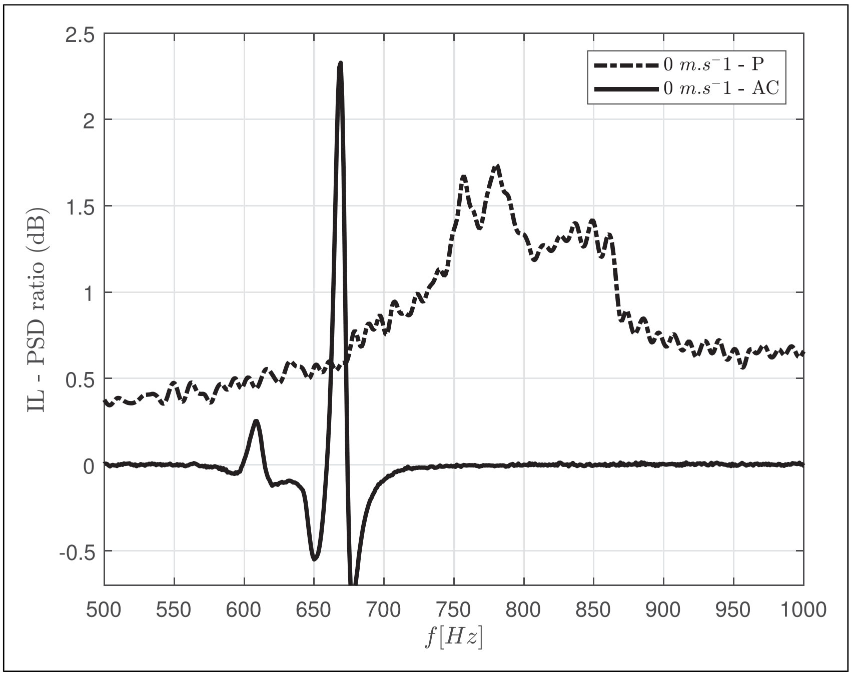

Figure 16. Comparison of the insertion loss IL in [dB] between the active and the passive materials without flow. P: passive material made of melamine foam covered with wire mesh.

frequency band corresponding to the identified controlled electromechanical mode.

This observation confirms that a future better-designed actuator with higher piezo acoustic coupling and larger bandwidth could offer better performance than passive solutions and use less space than hybrid systems with resonators.

6. Conclusion and perspectives

This paper presented experimental results on the early development of a newly designed active acoustic control system dedicated to stator vanes for jet engines consisting of flush-mounted piezoelectric cells. The idea behind this technological implementation was to control the noise created by turbulence interacting with the airfoil profile and also not disturb the airflow to maintain aerodynamic performance. As a first step toward the objective, three active cells have been placed into a wind tunnel with a primary acoustic source and an anechoic termination. Based on a modal identification of the piezo acoustic behavior of each cell, a linear MSISO controller has been designed to provide narrow-band rejection performance to the system due to its resonant characteristics. Thus, attenuation of 4 dB around the main controlled mode at 670 Hz has been achieved on the target downstream microphone PSD, increasing also the acoustic level on the upstream microphone as a side effect. A corresponding insertion loss of 2.5 dB has been reached for the considered bandwidth. The most interesting result is certainly that such performance level has been achieved with all values of experimented airflow velocities up to 20 $m.s^{-1}$. Since the proposed active control system is currently in an early prototyping phase, the actual results are modest. Nevertheless, they provide good confidence for a future better-designed actuator with higher piezo acoustic coupling to be able to control acoustic disturbances coming from real turbulence interacting with the vane leading edge.

Declaration of Conflicting Interests

The author(s) declared no potential conflicts of interest with respect to the research, authorship, and/or publication of this article.

Funding

The author(s) disclosed receipt of the following financial support for the research, authorship, and/or publication of this article: This project has received funding from the Clean Sky 2 Joint Undertaking (JU) under agreement n°865007. The JU receives support from the European Union's Horizon 2020 research and innovation program and the Clean Sky 2 JU members other than the Union. This publication reflects only the author's view and the JU is not responsible for any use that may be of the information it contains.

ORCID iD

Jonathan Rodriguez https://orcid.org/0000-0001-8872-8968

References

Bampanis G, Roger M and Moreau S (2022) On a three-dimensional investigation of airfoil turbulence-impingement noise and its reduction by leading-edge tubercles. *Journal of Sound and Vibration* 520: 116635.

Carmona JC and Alvarado VM (2000) Active noise control of a duct using robust control theory. *IEEE Transactions on Control Systems Technology* 8(6): 930–938.

Carneal JP, Giovanardi M, Fuller CR, et al. (2008) Re-Active Passive devices for control of noise transmission through a panel. *Journal of Sound and Vibration* 309(3-5): 495–506.

Curtis AR (1999) *Active Control of Fan Noise by Vane Actuators (No. E-11704)*. Cambridge, MA: GTE Internetworking Services.

Desquesnes G, Terracol M and Sagaut P (2007) Numerical investigation of the tone noise mechanism over laminar airfoils. *Journal of Fluid Mechanics* 591: 155–182.

Eldredge JD and Dowling AP (2003) The absorption of axial acoustic waves by a perforated liner with bias flow. *Journal of Fluid Mechanics* 485: 307–335.

Envia E (2002) Fan noise reduction: an overview. *International Journal of Aeroacoustics* 1(1): 43–64.

Envia E, Huff D and Morrison C (1996) Analytical assessment of stator sweep and lean in reducing rotor-stator tone noise. In: Aeroacoustics Conference, State College,PA, 06 May 1996, pp. 1791.

Galland MA, Mazeaud B and Sellen N (2005) *Hybrid passive/active absorbers for flow ducts. Applied acoustics* 66(6): 691–708.

Geyer T, Sarradj E and Fritzsche C (2010) Measurement of the noise generation at the trailing edge of porous airfoils. *Experiments in Fluids* 48(2): 291–308.

Hansen K, Kelso R and Doolan C (2012) *magenta*Reduction of flow induced airfoil tonal noise using leading edge sinusoidal modifications. *Acoustics Australia* 40(3): 172–177.

Huff DL (2002, September) Noise reduction technologies for turbofan engines *35th International Congress and Exposition on Noise Control Engineering*. Inter-Noise 2006).

Ingard KU and Dear TA (1985) Measurement of acoustic flow resistance. *Journal of Sound and Vibration* 103(4): 567–572.

Liu X, Zhao D, Guan D, et al. (2022) Development and progress in aeroacoustic noise reduction on turbofan aeroengines. *Progress in Aerospace Sciences* 130: 100796.

Neise W and Enghardt L (2003) Technology approach to aero engine noise reduction. *Aerospace Science and Technology* 7(5): 352–363.

Perez M, Ezzine M, Billon K, et al. (2020) Design and optimization of piezoelectric actuators for aeroacoustic noises control in a turbofan. In: *Smart Materials, Adaptive Structures and Intelligent Systems*. New York, NY: American Society of Mechanical Engineers, Vol. 84027, pp. V001T02A010.

Ripamonti F, Giampà A, Giona R, et al. (2022) Numerical and experimental study of an active control logic for modifying the acoustic performance of single-layer panels. *Journal of Sound and Vibration* 520: 116608.

Rodriguez J, Collet M and Chesné S (2021) Experimental modal identification of smart composite structure applied to active vibration control. *Smart Materials and Structures* 30(11): 115008.

Sellen N, Cuesta M and Galland MA (2006) Noise reduction in a flow duct: implementation of a hybrid passive/active solution. *Journal of Sound and Vibration* 297(3-5): 492–511.

Vemuri SS, Liu X, Zang B, et al. (2020) On the use of leading-edge serrations for noise control in a tandem airfoil configuration. *Physics of Fluids* 32(7): 077102.

Vinogradov I and Zhou Y (2014) Stator vane-based active control of turbofan engine noise *Fluid-Structure-Sound Interactions and Control*. Berlin, Heidelberg: Springer, pp. 247–252.